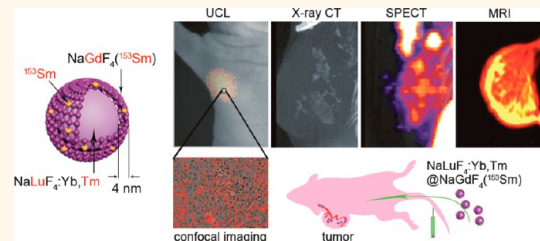


# Core–Shell Lanthanide Upconversion Nanophosphors as Four-Modal Probes for Tumor Angiogenesis Imaging

Yun Sun,<sup>†</sup> Xingjun Zhu,<sup>†</sup> Juanjuan Peng, and Fuyou Li\*

Department of Chemistry & The State Key Laboratory of Molecular Engineering of Polymers & Institutes of Biomedical Sciences, Fudan University, 220 Handan Road, Shanghai 200433, People's Republic of China. <sup>†</sup>These authors contributed equally.

**ABSTRACT** Multimodality imaging overcomes the shortage and incorporates the advantages of different imaging tools. Lanthanide-based nanoprobes are unique and have rich optical, magnetic, radioactive, and X-ray attenuation properties; however, simple doping of different lanthanide cations into one host can result in a material with multifunction but not the optimized properties. In this study, using  $\text{NaLuF}_4\text{-Yb,Tm}$  as the core and 4 nm of  $^{153}\text{Sm}^{3+}$ -doped  $\text{NaGdF}_4$  (half-life of  $^{153}\text{Sm} = 46.3$  h) as the shell, we developed a lanthanide-based core–shell nanocomposite as an optimized multimodal imaging probe with enhanced imaging ability. The lifetime of upconversion luminescence (UCL) at 800 nm and relaxation rate ( $1/T_1$ ) were at 1044  $\mu\text{s}$  and  $18.15 \text{ s}^{-1} \cdot \text{mM}^{-1}$ , respectively; however, no significant decrease in the attenuation coefficient was observed, which preserved the excellent X-ray imaging ability. The nanomaterial  $\text{NaLuF}_4\text{-Yb,Tm}@\text{NaGdF}_4(^{153}\text{Sm})$  was confirmed to be effective and applicable for UCL imaging, X-ray computed tomography (CT), magnetic resonance imaging, and single-photon emission computed tomography (SPECT) *in vivo*. Furthermore, the  $\text{NaLuF}_4\text{-Yb,Tm}@\text{NaGdF}_4(^{153}\text{Sm})$  nanoparticles were applied in tumor angiogenesis analysis by combining multimodality imaging of CT, SPECT, and confocal UCL imaging, which shows its value of multifunctional nanoparticles  $\text{NaLuF}_4\text{-Yb,Tm}@\text{NaGdF}_4(^{153}\text{Sm})$  in tumor angiogenesis imaging.



**KEYWORDS:** lanthanide · upconversion nanophosphor · multimodal imaging · tumor angiogenesis

Multimodality imaging has evoked considerable interest to circumvent the limitations of single imaging modes.<sup>1,2</sup> Single-photon emission computed tomography (SPECT) is a highly sensitive and quantitative translational tool but is limited in resolution (micrometer level) and provides no anatomical information.<sup>3</sup> Magnetic resonance imaging (MRI) is widely used to discriminate the infinitesimal change in soft tissues, and X-ray computed tomography (CT) displays a high degree of spatial resolution of the hard tissues (<50  $\mu\text{m}$ ).<sup>4</sup> MRI and X-ray CT are suitable for anatomical reconstruction but are not sensitive and lack molecular detail. Fluorescent imaging is suitable for multiscale imaging from the cellular level to whole-body animals but is hindered by a limited imaging depth of less than several centimeters. Many of the limitations of each of these techniques can be overcome by the use of a flexible multimodal platform which allows selection of the imaging modality to be used.

To achieve multifunction with radioactivity, magnetic, X-ray attenuation, and fluorescent properties, combining multiple contrast agents into a macromolecule or encapsulation of different probes into a special nanostructure (e.g., hollow nanosphere or mesoporous nanoparticle) has become a main strategy.<sup>1,5,6</sup> However, the radioactivity, magnetic, X-ray attenuation, and fluorescent properties originate from different molecules (or moieties), and the combination of all of these functions into one probe usually requires a complicated synthetic procedure and heterogeneous nanostructure. To the best of our knowledge, trimodal imaging is the upper limit of multimodal imaging in the previous studies.<sup>2,7</sup> Moreover, the introduction of an additional function is usually accompanied by a decrease in the original function. To date, although there are several reports of the application of multimodal probes *in vivo*, the imaging quality is limited due to unfavorable and fixed ratio of contrast agents in a single probe unit. The caveat is

\* Address correspondence to fyl@fudan.edu.cn.

Received for review September 30, 2013 and accepted November 8, 2013.

Published online November 08, 2013  
10.1021/nn405082y

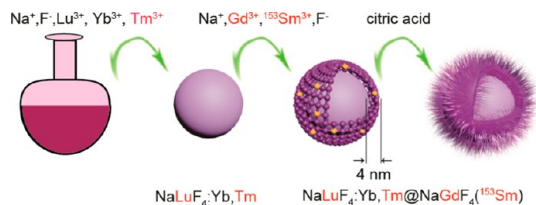
© 2013 American Chemical Society

that as the sensitivities of different imaging modalities can vary by 3 orders of magnitude, it may not be practical to simply add all functionalities to one molecule.<sup>1</sup>

Lanthanide nanoparticles provide rich optical, magnetic, radioactive, and X-ray attenuation properties by tuning the different 4f electronic structure of the lanthanide elements.<sup>8</sup> For example, due to the nature of heavy atoms, all lanthanide elements (from lanthanum to lutetium) have potential X-ray attenuation properties.<sup>9–11</sup> Gadolinium ions ( $Gd^{3+}$ ) possess seven unpaired electrons which can efficiently alter the relaxation time of surrounding water protons and have been widely used in MRI diagnosis of routine clinical disease.<sup>12</sup>  $^{153}Sm$  emits a gamma photon with a physical half-life of 46.3 h (1.93 days) and has been used in the clinic for radiotherapy and also as a SPECT imaging probe.<sup>13</sup> Moreover, using  $Yb^{3+}$  as the sensitizer and  $Er^{3+}$  (or  $Tm^{3+}$ ) as the activator, some nanoparticles have been developed which show intense upconversion luminescence (UCL) emission.<sup>14–21</sup> These lanthanide-based upconversion nanophosphors have been proved to have some significant advantages such as large anti-Stokes shift of several hundred nanometers, absence of autofluorescence from biological samples,<sup>22–24</sup> deep penetration depth,<sup>22,25</sup> and no photobleaching in luminescent bioimaging.<sup>26–29</sup> In light of the similar ionic radius and valence value, lanthanide cations can be easily doped into one host.<sup>30</sup> To date, several groups have developed dual-functional and trifunctional lanthanide-based nanoparticles with X-ray attenuation, magnetic, and (or) UCL properties.<sup>10,31–43</sup>

It should be noted that simple doping of these functional lanthanide cations into one host results in a material with multifunctions but not optimized properties. For example, Shi *et al.* reported that only the outside  $Gd^{3+}$  contributed to the  $T_1$ -enhanced MR effect, and doping  $Gd^{3+}$  into the whole host only provided a relatively low  $r_1$  value,<sup>44</sup> indicating that  $Gd^{3+}$  should be introduced in the outside layer. In contrast, the activator ( $Er^{3+}$  and  $Tm^{3+}$ ) should remain in the inner layer to avoid nonradiative transition because large defects exist in the outer surface of the nanoparticle.<sup>45,46</sup> For example, Prasad *et al.* have reported a kind of core–shell  $NaYbF_4: Tm @ NaGdF_4$  nanocrystal which presented bifunction of UCL and MR reflexivity.<sup>47</sup> Although  $NaYF_4$  has been considered a better host than  $NaGdF_4$ , the  $NaYF_4$  host displays weak X-ray attenuation properties. Therefore, it remains a challenge to design a nanocomposite structure with suitable host and doped ions using a general synthetic strategy in order to fabricate excellent multifunction nanomaterials for multimodality bioimaging.

In the present study, a lanthanide-based core–shell nanocomposite with radioactivity, magnetic, X-ray attenuation, and UCL properties was synthesized and applied in four-modality bioimaging of CT, MRI, SPECT,



**Scheme 1.** Schematic illustration of synthetic routine of the core–shell nanocomposite  $NaLuF_4: Yb, Tm @ NaGdF_4(153Sm)$ .

and UCL imaging *in vivo*. Our design strategy was based on the following: In our previous study, nanophosphors based on the  $NaLuF_4$  host showed an impressive quantum yield and significantly improved the UCL imaging effects,<sup>48</sup> and the  $NaLuF_4$ -based UCNPs could be used as an excellent X-ray CT contrast.<sup>49,50</sup> Therefore,  $NaLuF_4$  was used as the host and further codoped with 20%  $Yb$  and 1%  $Tm$  to achieve both UCL and X-ray CT imaging ability. To ensure  $Gd^{3+}$  in the outer layer, a 4 nm  $NaGdF_4$  layer as the shell was introduced onto the surface of  $NaLuF_4: Yb, Tm$  nanoparticles (Scheme 1). Moreover, radioactive  $^{153}Sm^{3+}$  was directly doped into the  $NaGdF_4$  shell. Such a core–shell nanostructure of  $NaLuF_4: Yb, Tm @ NaGdF_4(153Sm)$  provided excellent multifunction of an enhanced UCL emission, excellent X-ray attenuation,  $r_1$  value, and a gamma photon emissive radioactivity. Importantly, this core–shell  $NaLuF_4: Yb, Tm @ NaGdF_4(153Sm)$  nanocomposite was successfully developed as a new four-modal imaging nanoprobe to image the tumor angiogenesis.

## RESULTS AND DISCUSSION

**Synthesis and Characterization of the Nanocomposite.**  $NaLuF_4$  nanocrystals codoped with 20 mol % of  $Yb^{3+}$  and 1 mol % of  $Tm^{3+}$  were synthesized *via* a modified solvothermal method.<sup>51</sup> Herein, the as-prepared oleic acid (OA)-coated nanoparticles are denoted as OA- $NaLuF_4: Yb, Tm$ . As determined by transmission electron microscopy (TEM), the OA- $NaLuF_4: Yb, Tm$  nanoparticles had a spherical shape and an average size of  $\sim 13$  nm, as shown in Figure 1a–c. The peaks in the X-ray diffraction (XRD) patterns were well indexed to the hexagonal phase  $NaLuF_4$  (JCPDS No. 27-0736, Figure 1g). As previously reported,<sup>51–54</sup> the hexagonal phase of the  $NaLuF_4$  host achieved excellent UCL emission. The clear lattice fringes across the single particle in the high-resolution TEM (HRTEM) image show good crystallinity of the as-prepared nanocrystals, which also benefited UCL emission. The interplanar spacing of 0.50 nm also corresponded well to the  $d$ -spacing of the  $\{100\}$  facets of the hexagonal phase  $NaLuF_4$ .

To maximize the longitudinal relaxivity and to preserve enough Lu element in the host for high X-ray attenuation, a  $\sim 4$  nm  $NaGdF_4$  shell was coated onto the surface of OA- $NaLuF_4: Yb, Tm$  nanoparticles. At the same time, trace  $^{153}Sm$  (1850 MBq,  $7.4 \times 10^{-10}$  mol)

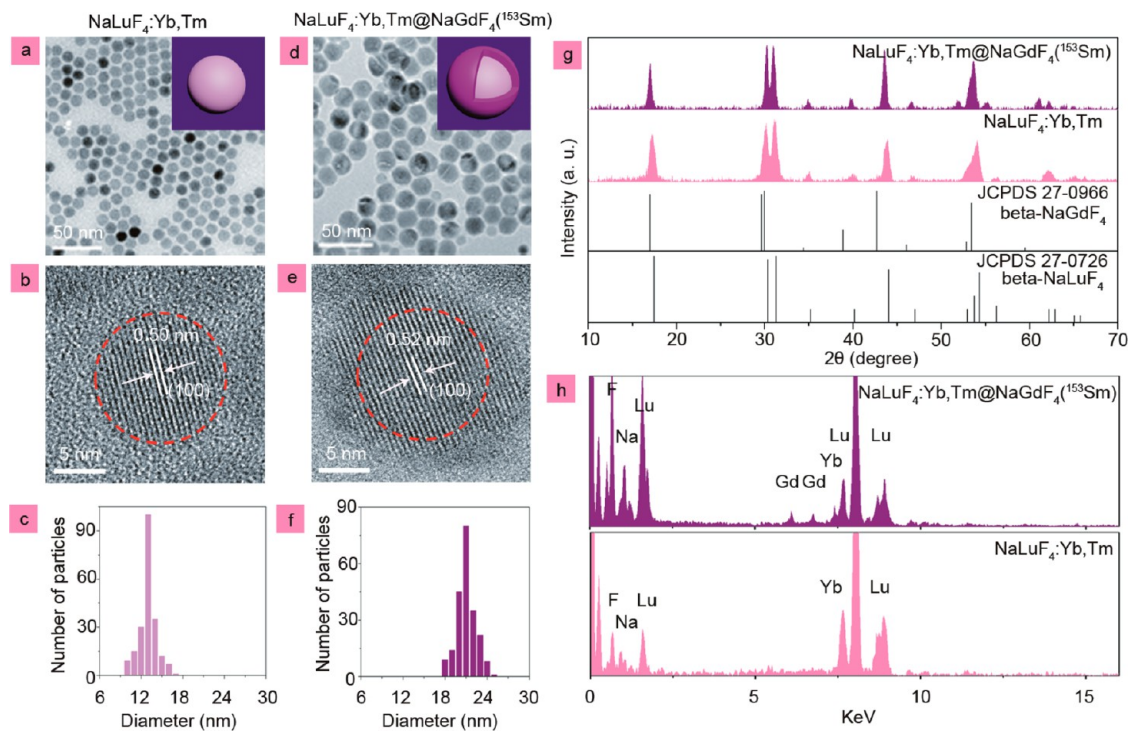


**Figure 1.** (a) TEM image and (b) enlarged TEM image and (c) size distribution of the  $\text{NaLuF}_4\text{:Yb,Tm}$ . (d) TEM image and (e) enlarged TEM image and (f) size distribution of the  $\text{NaLuF}_4\text{:Yb,Tm@NaGdF}_4\text{(}^{153}\text{Sm)}$ . (g) XRD pattern and (h) EDXA pattern of the  $\text{NaLuF}_4\text{:Yb,Tm}$  and  $\text{NaLuF}_4\text{:Yb,Tm@NaGdF}_4\text{(}^{153}\text{Sm)}$  nanoparticles.

was added in the synthetic procedure. The obtained nanoparticles were denoted as OA- $\text{NaLuF}_4\text{:Yb,Tm@NaGdF}_4\text{-}^{(153}\text{Sm)}$ . For further characterization and UCL/CT/MRI bioimaging experiments, the  $\text{NaLuF}_4\text{:Yb,Tm@NaGdF}_4\text{-}^{(153}\text{Sm)}$  samples were stored at least 20 days, until the radioactivity left cannot be detected by the radioactivity meter.

The core–shell nanostructure was confirmed by the increase in size and change in the energy-dispersive X-ray analysis (EDXA) results. As shown in Figure 1h, the EDXA indicated the presence of Lu elements in OA- $\text{NaLuF}_4\text{:Yb,Tm@NaGdF}_4\text{-}^{(153}\text{Sm)}$  compared with the OA- $\text{NaLuF}_4\text{:Yb,Tm}$  nanoparticles. The TEM observation indicated that the average size of OA- $\text{NaLuF}_4\text{:Yb,Tm@NaGdF}_4\text{-}^{(153}\text{Sm)}$  was  $\sim 21$  nm. Considering the size of  $\sim 13$  nm for the OA- $\text{NaLuF}_4\text{:Yb,Tm}$  nanoparticles (Figure 1c), the shell layer of  $\text{NaGdF}_4$  was evaluated to be  $\sim 4$  nm. The size ( $\sim 4$  nm) of the  $\text{NaGdF}_4$  shell matched the “negative lattice shielding effect” on  $\text{Gd}^{3+}$  ions reported by Shi *et al.*<sup>44</sup>

Furthermore, to achieve better dispersion of the nanoparticles in water, citric acid (cit) was used as a surface ligand to replace the surface OA ligand of the OA- $\text{NaLuF}_4\text{:Yb,Tm@NaGdF}_4\text{-}^{(153}\text{Sm)}$  through a process of ligand exchange.<sup>55</sup> The obtained cit-modified nanoparticles are described here as cit- $\text{NaLuF}_4\text{:Yb,Tm@NaGdF}_4\text{-}^{(153}\text{Sm)}$ . The cit- $\text{NaLuF}_4\text{:Yb,Tm@NaGdF}_4\text{-}^{(153}\text{Sm)}$  showed excellent water solubility, forming a clear colloidal solution, and was stable in suspension for 1 month at normal temperature and pressure

(Supporting Information Figure S1). Dynamic light scattering (DLS) indicated that the hydrodynamic diameter of the nanocomposite cit- $\text{NaLuF}_4\text{:Yb,Tm@NaGdF}_4\text{-}^{(153}\text{Sm)}$  was  $\sim 23$  nm (Figure S2), and the zeta-potential of the nanocomposite was measured to be about  $-18.4$  (Figure S3).

#### **NaLuF<sub>4</sub>:Yb,Tm@NaGdF<sub>4</sub>(<sup>153</sup>Sm) for UCL Bioimaging *In Vivo*.**

Under excitation from a CW 980 nm laser, the  $\text{NaLuF}_4\text{:Yb,Tm@NaGdF}_4\text{-}^{(153}\text{Sm)}$  in water showed two characteristic UCL emission bands centered at 475 and 800 nm (Figure 2a), originating from the  $^1\text{G}_4 \rightarrow ^3\text{H}_6$  and  $^3\text{H}_4 \rightarrow ^3\text{H}_6$  transitions of  $\text{Tm}^{3+}$ , respectively. In particular,  $\text{NaLuF}_4\text{:Yb,Tm@NaGdF}_4\text{-}^{(153}\text{Sm)}$  exhibited an intense near-infrared (NIR) UCL at 800 nm, providing 3.8-fold enhancement compared to the core of  $\text{NaLuF}_4\text{:Yb,Tm}$  with an equivalent luminescence center (Figure 2a), indicating the successful suppression of the nonradiative transition process. In addition, although the integrated intensity of UCL emission at 475 nm for  $\text{NaLuF}_4\text{:Yb,Tm@NaGdF}_4\text{-}^{(153}\text{Sm)}$  was significantly weaker than that at 800 nm, a blue UCL emission was still visible to the naked eye (Figure 2a inset), which indirectly indicated the excellent NIR emission at 800 nm of the core–shell nanocomposites.

In terms of upconversion materials, the UCL lifetimes were positively correlated with the quantum yield of UCL emission. The decay lifetimes of  $\text{NaLuF}_4\text{:Yb,Tm}$  and  $\text{NaLuF}_4\text{:Yb,Tm@NaGdF}_4\text{-}^{(153}\text{Sm)}$  were also investigated. The UCL lifetime of  $^3\text{H}_4 \rightarrow ^3\text{H}_6$  transitions of  $\text{Tm}^{3+}$  in  $\text{NaLuF}_4\text{:Yb,Tm@NaGdF}_4\text{-}^{(153}\text{Sm)}$  was  $1044 \mu\text{s}$

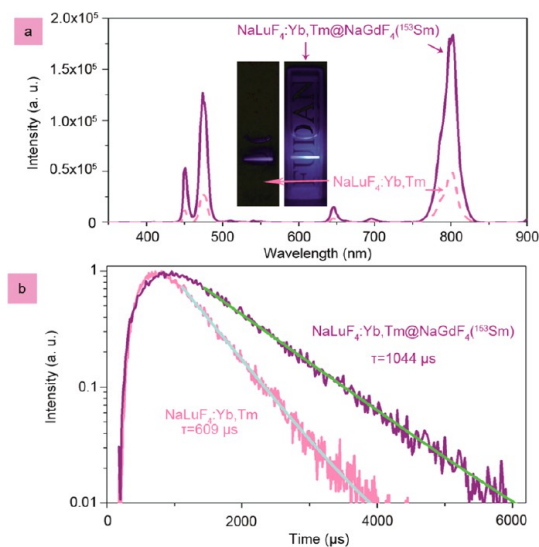


**Figure 2.** (a) UCL emission spectra of the NaLuF<sub>4</sub>:Yb,Tm and NaLuF<sub>4</sub>:Yb,Tm@NaGdF<sub>4</sub>(<sup>153</sup>Sm) in saline under excitation at 980 nm. Inset: Photo of UCL emission of the NaLuF<sub>4</sub>:Yb,Tm and NaLuF<sub>4</sub>:Yb,Tm@NaGdF<sub>4</sub>(<sup>153</sup>Sm), with a short-pass filter at 850 nm. (b) UCL lifetime of the powders of the NaLuF<sub>4</sub>:Yb,Tm and NaLuF<sub>4</sub>:Yb,Tm@NaGdF<sub>4</sub>(<sup>153</sup>Sm) at 800 nm under excitation at 980 nm.

(Figure 2b), which was longer than that ( $609 \mu\text{s}$ ) of NaLuF<sub>4</sub>:Yb,Tm. To ensure the UCL enhancement, quantum yield of the NaLuF<sub>4</sub>:Yb,Tm and the NaLuF<sub>4</sub>:Yb,Tm@NaGdF<sub>4</sub>(<sup>153</sup>Sm) was further measured. The absolute UCL quantum yields at  $^3\text{H}_4 \rightarrow ^3\text{H}_6$  (800 nm) of the powders of NaLuF<sub>4</sub>:Yb,Tm (13 nm) and NaLuF<sub>4</sub>:Yb,Tm@NaGdF<sub>4</sub>(<sup>153</sup>Sm) (21 nm) were  $0.28 \pm 0.05$  and  $1.02 \pm 0.05\%$ , respectively. This enhancement in UCL lifetime and quantum yield of the nanophosphors after coating a shell layer of NaGdF<sub>4</sub> is a result of a decrease in the nonradioactive transition of energy from the luminescence center to surface defects and surface ligands.<sup>45,46</sup>

In addition, 200  $\mu\text{L}$  of NaLuF<sub>4</sub>:Yb,Tm@NaGdF<sub>4</sub>(<sup>153</sup>Sm) (1 mg/mL) was injected intravenously into a mouse. After 30 min, the distribution of UCNPs within the mouse was investigated by our team using a modified UCL *in vivo* imaging system<sup>22</sup> upon irradiation by a CW 980 nm laser with a power density of 50 mW/cm<sup>2</sup>. The results showed no detectable noise from the skin or other organs, and the signal was mainly observed from the enterocoelia 30 min after injection. The peritoneum was then extirpated and imaged. Significant UCL emission was observed from the liver and spleen, whereas the other organs (such as heart, lung, kidney) showed no detectable UCL signals, indicating that the NaLuF<sub>4</sub>:Yb,Tm@NaGdF<sub>4</sub>(<sup>153</sup>Sm) was mainly distributed in the liver and spleen (Figure 3). The signal-to-noise ratio of UCL imaging was 21 (Figure S4). This observation was consistent with previous work.<sup>55,57</sup>

Due to the multiscale imaging ability of luminescence imaging, the process can be revealed by an optical confocal microscope. After sufficient disintegration of radioactive <sup>153</sup>Sm, the NaLuF<sub>4</sub>:Yb,

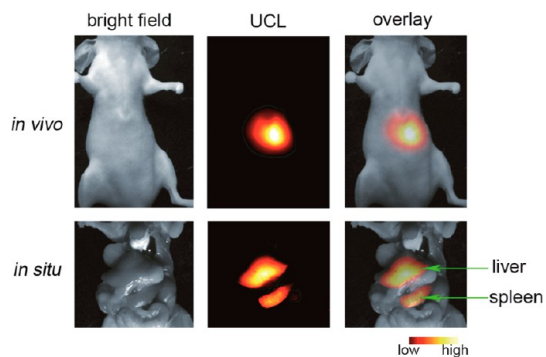


**Figure 3.** *In vivo* and *in situ* UCL imaging of the nude mice after intravenous injection of 200  $\mu\text{L}$  of NaLuF<sub>4</sub>:Yb,Tm@NaGdF<sub>4</sub>(<sup>153</sup>Sm) (1 mg/mL);  $\lambda_{\text{ex}} = 980 \text{ nm}$ ,  $\lambda_{\text{em}} = 800 \pm 10 \text{ nm}$ .

Tm@NaGdF<sub>4</sub>(<sup>153</sup>Sm) was interacted with macrophages. Interestingly, the macrophages could not endocytose the particle immediately after 1 h incubation, indicating that the nanocomposite was not initially captured by the mononuclear phagocytic system in the liver and spleen but may be a physical obstruction effect. Following incubation of the macrophages with NaLuF<sub>4</sub>:Yb,Tm@NaGdF<sub>4</sub>(<sup>153</sup>Sm) for 2 h, the particles entered the cells and were distributed in the cytoplasm (Figure S5).

**NaLuF<sub>4</sub>:Yb,Tm@NaGdF<sub>4</sub>(<sup>153</sup>Sm) for X-ray CT Imaging.** The X-ray attenuation coefficient is determined by the atomic number and electron density of the CT agent; the higher the atomic number and electron density are, the higher the attenuation coefficient is.<sup>58</sup> The atomic numbers and electron densities of lutetium (71 and 9.85 g/cm<sup>3</sup>, respectively), gadolinium (64 and 7.895 g/cm<sup>3</sup>, respectively), and ytterbium (70 and 6.98 g/cm<sup>3</sup>, respectively) are much higher than those of the currently used iodine (53 and 4.9 g/cm<sup>3</sup>). Therefore, it can be expected that NaLuF<sub>4</sub>:Yb,Tm@NaGdF<sub>4</sub>(<sup>153</sup>Sm) has an imaging ability in X-ray CT imaging.

To assess the X-ray imaging effect of NaLuF<sub>4</sub>:Yb,Tm@NaGdF<sub>4</sub>(<sup>153</sup>Sm), its X-ray attenuation was investigated. Different concentrations of NaLuF<sub>4</sub>:Yb,Tm@NaGdF<sub>4</sub>(<sup>153</sup>Sm) were monitored by X-ray CT to determine the HU value, using the control commercial X-ray imaging agent (lopromide injection solution) as the standard (Figure 4a,b). The results showed that the NaLuF<sub>4</sub>:Yb,Tm@NaGdF<sub>4</sub>(<sup>153</sup>Sm) solution at a concentration of 1 mg/mL was equivalent in X-ray attenuation to a 1.6 mg/mL lopromide injection solution (Figure 4a), indicating the excellent X-ray CT imaging ability of the nanocomposite and its potential as a CT imaging agent.

Furthermore, 1 h after intravenous injection of 800  $\mu\text{L}$  of NaLuF<sub>4</sub>:Yb,Tm@NaGdF<sub>4</sub>(<sup>153</sup>Sm) (30 mg/mL), the mouse was transferred into an X-ray CT system (Caliper Quantum FX). The resulting images are shown in Figure 4d,e, and the liver and spleen of the nanocomposite-treated mouse showed significant X-ray attenuation compared to the control mouse without

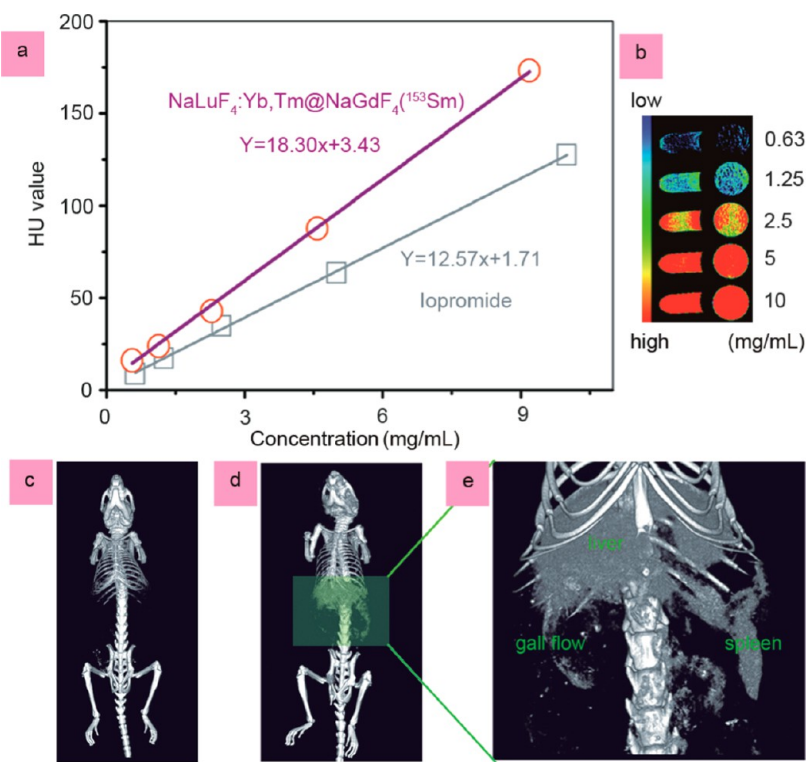


**Figure 4.** (a) HU value at various concentrations of lopromide (gray) and NaLuF<sub>4</sub>:Yb,Tm@NaGdF<sub>4</sub>(<sup>153</sup>Sm) (red) at room temperature detected by X-ray CT. (b) X-ray CT imaging of the NaLuF<sub>4</sub>:Yb,Tm@NaGdF<sub>4</sub>(<sup>153</sup>Sm) solution with different concentrations of 0.63–10 mg mL<sup>-1</sup>. (c) X-ray CT imaging of the control mouse without injection of NaLuF<sub>4</sub>:Yb,Tm@NaGdF<sub>4</sub>(<sup>153</sup>Sm). (d) X-ray CT imaging of the mouse after intravenous injection of 800  $\mu$ L of NaLuF<sub>4</sub>:Yb,Tm@NaGdF<sub>4</sub>(<sup>153</sup>Sm) (30 mg/mL). (e) X-ray CT imaging focused on the peritoneum.

injection of NaLuF<sub>4</sub>:Yb,Tm@NaGdF<sub>4</sub>(<sup>153</sup>Sm) (Figure 4c). Interestingly, the bile flow from the gall bladder to the intestine was also observed on X-ray CT, whereas no obvious signal in the urinary bladder was observed, clearly indicating that the main excretion of NaLuF<sub>4</sub>:Yb,Tm@NaGdF<sub>4</sub>(<sup>153</sup>Sm) was *via* the gall to the intestine.

**NaLuF<sub>4</sub>:Yb,Tm@NaGdF<sub>4</sub>(<sup>153</sup>Sm) for *In Vivo* MR Imaging.** Paramagnetic Gd<sup>3+</sup> with seven unpaired electrons has been proved to be an excellent contrast agent for MRI. Moreover, recent results indicated that the inner Gd<sup>3+</sup> displayed weak longitudinal relaxivity. For example, Lee's group found that the relaxivities of paramagnetic Gd<sub>2</sub>O<sub>3</sub> nanoparticles with increased nanoparticle size, from 1.0 to 30 nm, showed an obvious decrease in longitudinal relaxivities, from 9.9 to 0.1 mM<sup>-1</sup> s<sup>-1</sup>.<sup>38</sup> Shi *et al.* observed nearly 100% loss of longitudinal relaxivity of Gd<sup>3+</sup> ions buried deep (>4 nm) within crystal lattices.<sup>44</sup> Therefore, in our study, a ~4 nm NaGdF<sub>4</sub> shell was introduced onto the upconversion nanophosphor core to maximize the longitudinal relaxivity. As determined on a 3 T MRI scanner, the relaxivity parameter (*r*<sub>1</sub>), calculated from the slope of the concentration-dependent relaxation rate (1/*T*<sub>1</sub>) was 18.15 s<sup>-1</sup> · mM<sup>-1</sup> (Figure 5a), which was significantly higher than that (5.6 s<sup>-1</sup> · mM<sup>-1</sup>) of our reported pure NaGdF<sub>4</sub> nanoparticle (25–55 nm).<sup>56</sup> This increase in *r*<sub>1</sub> value was

attributed to more Gd<sup>3+</sup> in the outer layer of the nanocomposite and thus more Gd<sup>3+</sup> interactions with water protons.

Compared to other imaging methods, MRI can reveal more details of soft tissues to help researchers identify the nidus more precisely and distinguish the nidus from other soft tissues. Herein, to confirm the *in vivo* effectiveness of NaLuF<sub>4</sub>:Yb,Tm@NaGdF<sub>4</sub>(<sup>153</sup>Sm), a mouse was injected intravenously with NaLuF<sub>4</sub>:Yb,Tm@NaGdF<sub>4</sub>(<sup>153</sup>Sm) (800  $\mu$ L, 30 mg/mL) and transferred to a 9.4 T MRI scanner 1 h later. As shown in Figure 5b,c, *T*<sub>1</sub>-weighted transverse cross-sectional images of the nanocomposite-treated mouse showed significant contrast enhancement in the liver and spleen area after intravenous injection of NaLuF<sub>4</sub>:Yb,Tm@NaGdF<sub>4</sub>(<sup>153</sup>Sm).

#### NaLuF<sub>4</sub>:Yb,Tm@NaGdF<sub>4</sub>(<sup>153</sup>Sm) for *In Vivo* SPECT Imaging.

Due to the introduction of the radioactive <sup>153</sup>Sm element, it is expected that NaLuF<sub>4</sub>:Yb,Tm@NaGdF<sub>4</sub>(<sup>153</sup>Sm) could be applied in SPECT imaging. To confirm the purity and stability of doping, NaLuF<sub>4</sub>:Yb,Tm@NaGdF<sub>4</sub>(<sup>153</sup>Sm) was incubated in fetal bovine serum (FBS) and then monitored by radiochromatography using a TLC scanner. In the control, <sup>153</sup>Sm<sup>3+</sup> moved quickly in the silica-gel-coated TLC plates (black, Figure 6). As shown in Figure 6, almost all of the signal for the nanocomposite remained at the start point when the solution arrived at the front of the

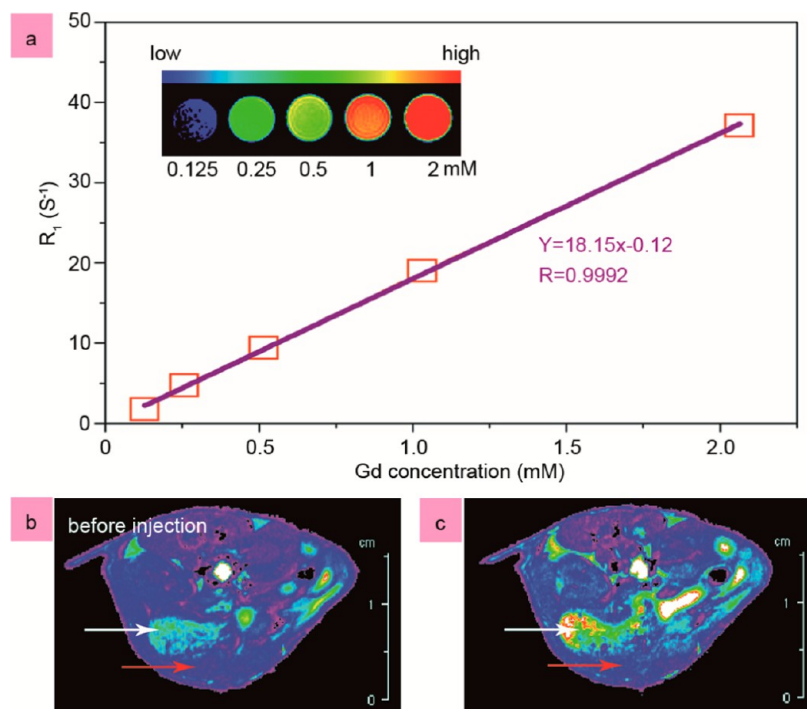


**Figure 5.** (a) Relaxation rate  $R_1$  ( $1/T_1$ ) versus various concentrations of hydrophilic  $\text{NaLuF}_4\text{:Yb,Tm@NaGdF}_4(^{153}\text{Sm})$  at room temperature using a 3 T MRI scanner. MR imaging of the mouse before (b) and after (c) intravenous injection of  $800 \mu\text{L}$  of  $\text{NaLuF}_4\text{:Yb,Tm@NaGdF}_4(^{153}\text{Sm})$  ( $30 \text{ mg/mL}$ ), using a 9.4 T MRI scanner (Bruker). The red arrow indicates the liver, and the white arrow indicates the spleen. RARE sequence was used for MR imaging. TR =  $395.2 \text{ ms}$ , TE =  $8.1 \text{ ms}$ .

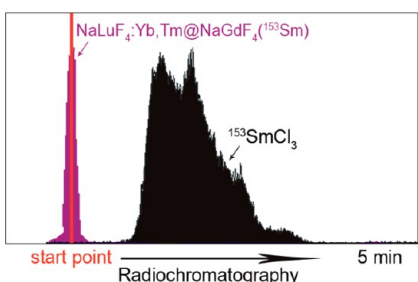


**Figure 6.** Radiochromatography data of  $\text{NaLuF}_4\text{:Yb,Tm@NaGdF}_4(^{153}\text{Sm})$  (purple) and  $^{153}\text{SmCl}_3$  (black) in the stability study after incubation in fetal bovine serum.

plate, indicating negligible dissociation of  $^{153}\text{Sm}^{3+}$  from the nanocomposites.

To further verify the *in vivo* effectiveness, the mouse was injected with  $200 \mu\text{L}$  of  $\text{NaLuF}_4\text{:Yb,Tm@NaGdF}_4(^{153}\text{Sm})$  ( $148 \text{ MBq}$ ,  $1 \text{ mg/mL}$ ) intravenously and then imaged using a small animal SPECT/CT system over 24 h. Consistent with the results of UCL and X-ray CT imaging, the radioactive signal was mainly located in the liver and spleen of the mouse. Moreover, the distribution sites were unchanged, but the signal in the liver decreases quickly with time (Figure 7a). However, UCL, MRI, and X-ray CT imaging did not provide quantification of the biodistribution of the nanocomposite.

Quantification of the biodistribution of  $\text{NaLuF}_4\text{:Yb,Tm@NaGdF}_4(^{153}\text{Sm})$  in a living mouse was investigated. As shown in Figure 7b, 1 h after intravenous

injection, radioactive signals from the liver and spleen were highest, indicating that most of the nanocomposite was immediately distributed in the liver and spleen after injection. Moreover, 1 h after injection,  $\sim 74\%$  of the injected dose was found in the liver and spleen ( $\sim 1.7 \text{ mg}$  in liver and  $0.15 \text{ mg}$  in spleen). The ratio of radioactivity concentration (%ID/g) of  $^{153}\text{Sm}$  in liver to spleen was  $\sim 1.7:1$ . The  $^{153}\text{Sm}$  signal in liver and spleen further decreased up to 24 h after injection. Moreover, although  $^{153}\text{Sm}^{3+}$  is also a bone imaging agent, no significant detectable  $^{153}\text{Sm}$  signal was found in bone 24 h after injection, indicating no significant release of  $^{153}\text{Sm}^{3+}$  ions from the  $\text{NaLuF}_4\text{:Yb,Tm@NaGdF}_4(^{153}\text{Sm})$  nanocomposite within the living mouse. At 60 h after injection, the  $^{153}\text{Sm}$  signals from the liver and spleen showed a  $55.75$  and  $15.56\%$  loss in dose and a  $55.85$  and  $15.45\%$  loss in concentration, respectively. Clearly, all  $\text{NaLuF}_4\text{:Yb,Tm@NaGdF}_4(^{153}\text{Sm})$  in liver and spleen was prone to be excreted from the body.

These above-mentioned results show the successful construction of a four-modal imaging agent and more information of distribution of this agent  $\text{NaLuF}_4\text{:Yb,Tm@NaGdF}_4(^{153}\text{Sm})$  from different sides than previous studies.

**Four-Modal Imaging of Tumor Angiogenesis Using  $\text{NaLuF}_4\text{:Yb,Tm@NaGdF}_4(^{153}\text{Sm})$  as a Probe.** Solid tumors less than  $1 \text{ mm}^3$  are not vascularized. To spread, the tumor needs angiogenesis that new blood vessels form from pre-existing vessels. Malignancy in cancer was positively correlated with the degree of angiogenesis,<sup>59,60</sup> and

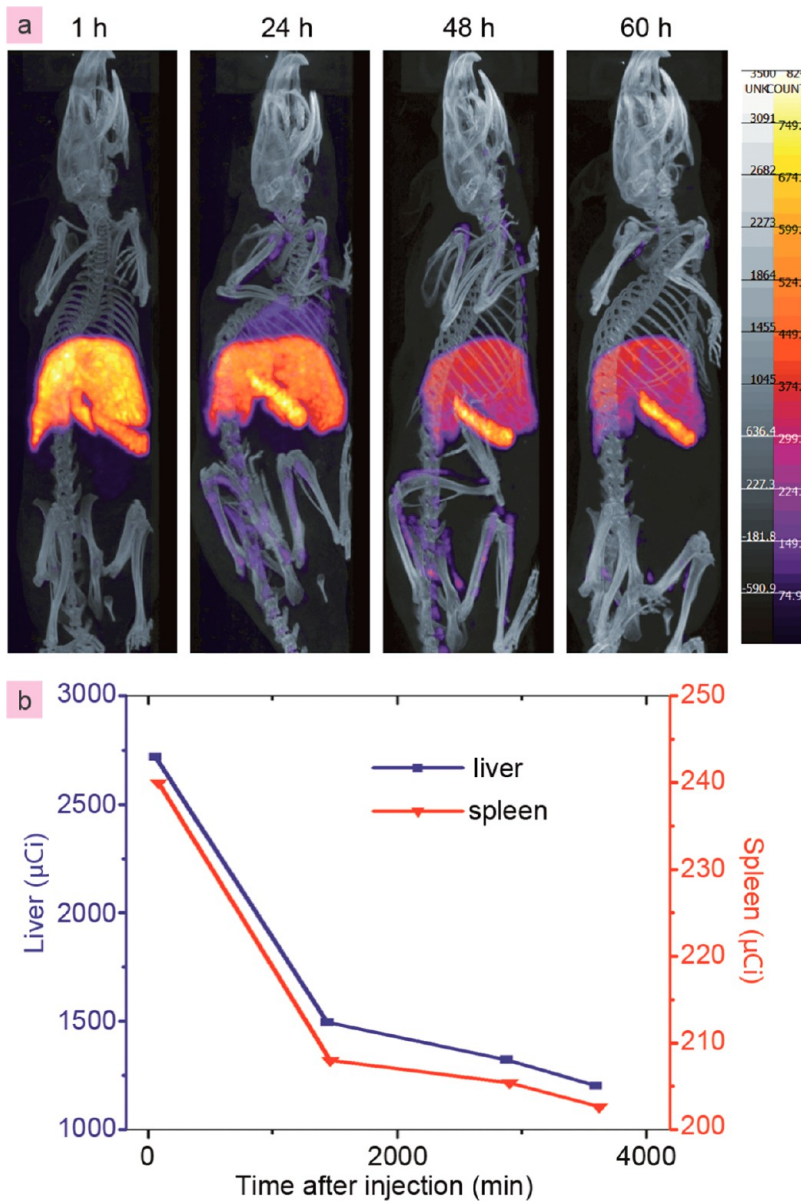


**Figure 7.** (a) SPECT/CT imaging of a living mouse following intravenous injection of  $200\ \mu\text{L}$  of  $\text{NaLuF}_4\text{-Yb,Tm@NaGdF}_4\text{-}^{153}\text{Sm}$  ( $\sim 12.5\ \text{mg/mL}$ ) at different time points (1, 12, 24, 48 h). (b) Quantification of the radioactive dose in liver and spleen of the mouse injected with  $\text{NaLuF}_4\text{-Yb,Tm@NaGdF}_4\text{-}^{153}\text{Sm}$  intravenously at different time points. All data were processed with an attenuation correction.

thus tumor angiogenesis imaging can allow for much earlier diagnosis and better prognosis.<sup>61</sup> Multimodal imaging combined multifunctional probes can yield complementary information and offer synergistic advantages over any modality alone.<sup>62–65</sup> Herein, the availability and effects of  $\text{NaLuF}_4\text{-Yb,Tm@NaGdF}_4\text{-}^{153}\text{Sm}$  as a multifunctional probe for tumor angiogenesis imaging *in vivo* were tested on KB human oral tumor-bearing nude mouse (Figure S6). One hour after intravenous injection of  $\text{NaLuF}_4\text{-Yb,Tm@NaGdF}_4\text{-}^{153}\text{Sm}$ , the tumor-grafted nude mouse was imaged with UCL, X-ray CT, MRI, and SPECT imaging devices, and the bioimaging results are shown in Figure 8.

X-ray CT imaging focused on the tumor showed tube-like structure in the tumor with high attenuation

of X-ray (Figure 8b), indicating the distribution of  $\text{NaLuF}_4\text{-Yb,Tm@NaGdF}_4\text{-}^{153}\text{Sm}$  in the tumor blood vessel. In addition, the sparse distribution of blood vessels indicated the moderate angiogenesis and malignancy in the tumor. Considering that MRI is usually used to monitor the details of soft tissue, the MRI image of the tumor-grafted nude mouse injected with  $\text{NaLuF}_4\text{-Yb,Tm@NaGdF}_4\text{-}^{153}\text{Sm}$  was investigated. The MRI image showed intense signals in the peripheral moiety of the tumor (Figure 8d), which was distinguished from the observation of X-ray CT imaging in the tumor. This fact indicated that the MRI result is easily interfered with by a false positive signal from normal tissues such as fat with a short relaxation time  $T_1$ ,<sup>66</sup> and that multimodal imaging is necessary in visualization of tumor angiogenesis.

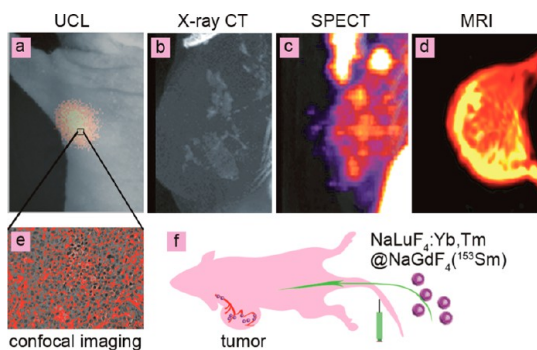


**Figure 8.** (a–d) Four-modal imaging of the focused tumor from the tumor-bearing nude mouse 1 h after intravenous injection of  $\text{NaLuF}_4\text{:Yb,Tm@NaGdF}_4(^{153}\text{Sm})$ . (a) *In vivo* UCL-image, (b) X-ray CT image, (c) SPECT image, (d) MR imaging of tumor. (e) UCL confocal image of the paraffin section of tumor tissue. (f) Schematic illustration of tumor angiogenesis imaging using  $\text{NaLuF}_4\text{:Yb,Tm@NaGdF}_4(^{153}\text{Sm})$  as the probe.

Quantification information is very important for judgment of the degree of angiogenesis. Although the resolution of SPECT image was much poorer than that of X-ray CT, SPECT imaging has its advantage of absolute quantification imaging ability. As shown in Figure 8c, SPECT imaging demonstrated intense signal in the tumor region. Analysis of SPECT imaging data showed that ~1.7% of injected dose of the  $\text{NaLuF}_4\text{:Yb,Tm@NaGdF}_4(^{153}\text{Sm})$  was within the tumor.

Furthermore, the UCL imaging was applied in histochemistry analysis of tumor angiogenesis, in spite of low penetration depth of UCL imaging *in vivo* (Figure 8a). The UCL confocal imaging of the paraffin section of tumor tissue showed intense UCL signals in the intercellular space of tumor tissue, indirectly

indicating the leakage of upconversion nanoparticles from the tumor vasculature and thus permeable and fractured blood vessels of the tumor (Figure 8e).

All above-mentioned data indicated that the information from each image was limited and that multimodal imaging benefited the tumor angiogenesis imaging through a combination of complementary four modalities to reveal more details. Therefore, it can safely be concluded that the availability of  $\text{NaLuF}_4\text{:Yb,Tm@NaGdF}_4(^{153}\text{Sm})$  as an excellent multimodal probe for tumor angiogenesis imaging was proved.

## CONCLUSIONS

In summary, we demonstrated that the synthesis of core–shell nanocomposite  $\text{NaLuF}_4\text{:Yb,Tm@NaGdF}_4(^{153}\text{Sm})$  constituted a hexagonal  $\text{NaLuF}_4\text{:Yb,Tm}$  nanocrystal as the core and a 4 nm  $^{153}\text{Sm}^{3+}$ -doped  $\text{NaGdF}_4$  as the shell and its application as a four-modal imaging nanoprobe for CT, MRI, SPECT, and UCL imaging. Using this nanocomposite  $\text{NaLuF}_4\text{:Yb,Tm@NaGdF}_4(^{153}\text{Sm})$  as a probe, we realized four-modal imaging (UCL, CT, MRI, SPECT) in a small animal and achieved detailed information on the distribution from the cell to whole-body level, distribution in different soft tissues, dynamic long-term quantification data, and 3D information. Moreover, this nanocomposite  $\text{NaLuF}_4\text{:Yb,Tm@NaGdF}_4(^{153}\text{Sm})$  has been applied in tumor angiogenesis imaging. Therefore, this four-modal imaging probe provides a new strategy for the fabrication of multifunctional nanocrystals for further applications in biological science and medicine, and both researchers and clinicians could easily combine the functions needed to achieve more accurate information.

## MATERIALS AND METHODS

**Materials.** All the starting materials were obtained from commercial suppliers and used as received. Rare-earth oxides  $\text{Lu}_2\text{O}_3$  (99.999%),  $\text{Yb}_2\text{O}_3$  (99.999%),  $\text{Gd}_2\text{O}_3$  (99.999%), and  $\text{Tm}_2\text{O}_3$  (99.98%) were purchased from Shanghai Yuelong New Materials Co. Ltd. Oleic acid (>90%) was purchased from Alfa Aesar Co., Ltd. 1-Octadecene (ODE) (>90%) was purchased from Aladdin Reagent Co., Ltd.  $\text{NaOH}$ ,  $\text{NH}_4\text{F}$ , methanol, ethanol, cyclohexane, and hydrochloric solution were purchased from Sinopharm Chemical Reagent Co., China. Rare-earth chlorides ( $\text{LnCl}_3$ ,  $\text{Ln}$ :  $\text{Lu}$ ,  $\text{Yb}$ ,  $\text{Gd}$ , and  $\text{Tm}$ ) were prepared by dissolving the corresponding metal oxide in 10% hydrochloric solution at elevated temperature and then evaporating the water completely. All other chemical reagents were of analytical grade and were used directly without further purification. Deionized water was used throughout the experiments.  $^{153}\text{SmCl}_3$  solution was purchased from the HTA Co., Ltd., China.

**Characterization.** Powder X-ray diffraction (XRD) measurements were performed on a Bruker D4 diffractometer at a scanning rate of 1°/min in the  $2\theta$  range from 10 to 70° (Cu  $\text{K}\alpha$  radiation,  $\lambda = 1.54056 \text{ \AA}$ ). The size and morphology of UCNPs were determined at 200 kV at a JEOL JEM-2010 low- to high-resolution transmission electron microscope (HRTEM). These as-prepared samples were dispersed in cyclohexane and dropped on the surface of a copper grid for the TEM test. The UCL spectrum was recorded on Edinburgh FLS-920 instrument, but

the excitation source used an external 0–1 W adjustable 980 nm semiconductor laser (Shanghai Hi-Tech Optoelectronic Co., China) with an fiber optic accessory, instead of the xenon source in the spectrophotometer. All the photoluminescence studies were carried out at room temperature. The photo of UCL emission was obtained digitally on a Nikon multiple CCD camera. Fluorescence spectroscopy (Edinburgh LFS920) modified with NIR PMT (Hamamatsu, C9940-02, No. CA0142) as detector was used to detect the excitation light from continuous-wave 980 nm laser (0–8 W) and upconversion luminescence (800 nm) from  $\text{Tm}^{3+}$  for quantum yield measurement.

**Synthesis of Oleic Acid (OA)-Capped  $\text{NaLuF}_4\text{:Yb,Tm@NaGdF}_4(^{153}\text{Sm})$  Core–Shell Nanocrystals.**  $\text{NaLuF}_4\text{:Yb,Tm}$  core nanoparticles were prepared with a solvothermal method. Typically, 0.1 mmol  $\text{LnCl}_3$  ( $\text{RE} = \text{Lu, Yb, Tm}$ ) with the molar ratio of 79:20:1 was mixed with 0.6 mL of oleic acid and 1.5 mL of 1-octadecene (ODE). The mixture was heated to 140 °C for 30 min to obtain a clear solution and then cooled to room temperature. One milliliter methanol solution of  $\text{NH}_4\text{F}$  (0.4 mmol) and  $\text{NaOH}$  (0.25 mmol) was added into the bottle. After being stirred at 100 °C for 20 min to remove methanol, the solution was heated to 300 °C under argon for 1 h. After being cooled to room temperature, nanoparticles were precipitated by 2 mL of ethanol and collected by centrifugation. After being washed with ethanol and cyclohexane several times, OA- $\text{NaLuF}_4\text{:Yb,Tm}$  nanocrystals were stored in 1 mL of cyclohexane for the next step.

Similarly, OA-NaLuF<sub>4</sub>:Yb,Tm@NaGdF<sub>4</sub>(<sup>153</sup>Sm) core–shell nanoparticles were synthesized by a modified solvothermal method. First, 0.05 mmol GdCl<sub>3</sub> and 1850 MBq <sup>153</sup>SmCl<sub>3</sub> (7.4 × 10–10 mol) were added into 0.6 mL of oleic acid and 1.5 mL of ODE and heated to 140 °C for 30 min to obtain a clear solution and then cooled to room temperature. One milliliter of cyclohexane solution of NaLuF<sub>4</sub>:Yb,Tm nanocrystals was added dropwise into the solution. The mixture was degassed at 80 °C for 20 min to remove cyclohexane and cooled to room temperature. Then 1 mL methanol solution of NH<sub>4</sub>F (0.4 mmol) and NaOH (0.25 mmol) was added. After being stirred at 100 °C for 20 min to remove methanol, the solution was heated to 300 °C under argon for 1 h. After being cooled to room temperature, nanoparticles were precipitated by 2 mL of ethanol and collected by centrifugation and then washed with ethanol and cyclohexane several times.

**Synthesis of Water-Soluble NaLuF<sub>4</sub>:Yb,Tm@NaGdF<sub>4</sub>(<sup>153</sup>Sm) Core–Shell Nanocrystals Modified by Citrate.** The preparation of the water-soluble NaLuF<sub>4</sub>:Yb,Tm@NaGdF<sub>4</sub>(<sup>153</sup>Sm) nanocrystals was performed as reported by Nicoleta and Carpenter.<sup>67</sup> First, the 10 mg of OA-NaLuF<sub>4</sub>:Yb,Tm@NaGdF<sub>4</sub>(<sup>153</sup>Sm) was washed with pH = 4 hydrochloric acid to obtain water-dispersible, ligand-free NaLuF<sub>4</sub>:Yb,Tm@NaGdF<sub>4</sub>(<sup>153</sup>Sm). Then, ligand-free NaLuF<sub>4</sub>:Yb,Tm@NaGdF<sub>4</sub>(<sup>153</sup>Sm) was collected and redispersed in the 10 mg/mL citrate acid solution, and the NaLuF<sub>4</sub>:Yb,Tm@NaGdF<sub>4</sub>(<sup>153</sup>Sm) was obtained. Then, the cit-NaLuF<sub>4</sub>:Yb,Tm@NaGdF<sub>4</sub>(<sup>153</sup>Sm) was washed with water three times.

**X-ray Attenuation of NaLuF<sub>4</sub>:Yb,Tm@NaGdF<sub>4</sub>(<sup>153</sup>Sm).** Different concentration of NaLuF<sub>4</sub>:Yb,Tm@NaGdF<sub>4</sub>(<sup>153</sup>Sm) (complete disintegration) and the control commercial X-ray imaging agents, iopromide injection solution, was monitored by X-ray CT to determine the specification curve of the HU value.

**Relaxivity ( $r_1$ ) of NaLuF<sub>4</sub>:Yb,Tm@NaGdF<sub>4</sub>(<sup>153</sup>Sm).** The  $T_1$ -weighted MR images were obtained using a 3T Siemens Magnetom Trio running in conjunction with an 8 array loop coil (Siemens Medical Systems). Dilutions of NaLuF<sub>4</sub>:Yb,Tm@NaGdF<sub>4</sub>(<sup>153</sup>Sm) in deionized water were placed in a series of 1.5 mL tubes for  $T_1$ -weighted MR imaging. The following parameters were adopted.  $T_1$ -weighted sequence: saturation recover (SR), TR/TE = 620/8.9 ms, matrix = 256 × 256, FOV = 130 × 130, slice thickness = 2.0 mm. Paramagnetic contrast agents were measured for relaxivity with a 3T Siemens Magnetom Trio.  $T_1$ -weighted contrast enhancement was performed running a standard inversion recovery (IR) spin–echo sequence with a repetition time (TR) of 6500 ms, an echo time (TE) of 7.6 ms, and 10 inversion recovery times (inversion time (TI) = 23, 100, 200, 250, 300, 400, 800, 1200, 2000, and 3000 ms). The acquired images had a matrix size of 256 × 256, a field of view of 200 × 200 mm, and a slice thickness of 3.0 mm. The data were collected and analyzed using Siemens' Syngo software. The MR signal intensity in tubes was ascertained by the average intensity in the defined regions of interests (ROIs).  $T_1$  values of each tube were calculated using the following formula:  $S(TI) = S_0 \times [1 - 2 \exp(-TI/T_1)]$  to fit the  $T_1$  recovery curve in the circular regions of interest for each sample. The resulting  $T_1$  values were averaged over the region of interest and plotted as  $1/T_1 (r_1)$  versus molar concentration of UCNPs. The slopes of these lines provide the molar relaxivity  $r_1$ .

**Stability of the <sup>153</sup>Sm Labeling.** The NaLuF<sub>4</sub>:Yb,Tm@NaGdF<sub>4</sub>(<sup>153</sup>Sm) was incubated with fetal bovine serum (FBS) for 2 h and then monitored by radiochromatography using a TLC scanner. <sup>153</sup>SmCl<sub>3</sub> was set as control and monitored by radiochromatography.

**UCL Imaging.** The NaLuF<sub>4</sub>:Yb,Tm@NaGdF<sub>4</sub>(<sup>153</sup>Sm) in 200  $\mu$ L of saline (1 mg/mL) was subcutaneously injected *via* tail vein to a 4 week old nude mouse. One hour later, the mouse was anesthetized and then imaged by our setup UCL *in vivo* imaging system,<sup>22</sup> only by collecting the UCL at 800 nm with a EMCCD upon irradiation by CW 980 nm laser (50 mW/cm<sup>2</sup>). After that, the peritoneum was exenterated and then the organs were imaged *in situ*.

**UCL Imaging of Macrophages Incubated with NaLuF<sub>4</sub>:Yb,Tm@NaGdF<sub>4</sub>(<sup>153</sup>Sm).** The macrophages were provided by the Institute of Biochemistry and Cell Biology, SIBS, CAS (China). The macrophages were grown in DMEM (Dulbecco's modified Eagle's medium) supplemented with 10% FBS.

Cells (5 × 10<sup>5</sup>/mL) were plated on 14 mm glass coverslips and allowed to adhere for 24 h. The cells were washed with PBS and then incubated with 100  $\mu$ g/mL NaLuF<sub>4</sub>:Yb,Tm@NaGdF<sub>4</sub>(<sup>153</sup>Sm) (after sufficient disintegration of radioisotopes) for 2 h at 37 °C. Cell imaging was then carried out on a laser scanning UCL microscope after washing the cells with PBS.<sup>23</sup>

**CT Imaging.** The mouse was intravenously injected with 800  $\mu$ L of NaLuF<sub>4</sub>:Yb,Tm@NaGdF<sub>4</sub>(<sup>153</sup>Sm) (30 mg/mL) and 1 h later imaged by a small animal X-ray CT (Quantum FX). A scan lasted about 1 min. A modified Feldkamp algorithm, using undersampling to reduce noise, was applied to the scan data, resulting in reconstructed 3D data sets with a voxel size of 20  $\mu$ m.

**MRI Imaging.** The mouse was first imaged by a 9.4 T Bruker MRI scanner using a  $T_1$ -weighted RARE sequence (TR = 395.2 ms, TE = 81 ms, 256 × 256 matrix, slice thickness = 2.0 mm). Then, 800  $\mu$ L of NaLuF<sub>4</sub>:Yb,Tm@NaGdF<sub>4</sub>(<sup>153</sup>Sm) (30 mg/mL) was intravenously injected to the mouse *via* tail vein and imaged by the MRI.

**SPECT/CT Imaging.** The mouse was intravenously injected with 200  $\mu$ L of NaLuF<sub>4</sub>:Yb,Tm@NaGdF<sub>4</sub>(<sup>153</sup>Sm) (148 MBq) with a concentration of 12.5 mg/mL and then imaged by a small animal SPECT/CT (Bioscan) at 1, 24, 48, and 60 h after injection. Quantification, fusion, and 3D reconstruction was performed by InVivoScope software. All data have been processed with attenuation correction.

**Tumor Model.** KB cells (10<sup>6</sup>) were grafted into the nude mouse, and 14 days later, the tumor with a size of ~1 cm was formed.

**Four-Modal Imaging of Tumor Angiogenesis Using NaLuF<sub>4</sub>:Yb,Tm@NaGdF<sub>4</sub>(<sup>153</sup>Sm) as a Probe.** Another 5 mg of NaLuF<sub>4</sub>:Yb,Tm@NaGdF<sub>4</sub>(<sup>153</sup>Sm) was postlabeled in 1 mL of saline. Then, 200  $\mu$ L of NaLuF<sub>4</sub>:Yb,Tm@NaGdF<sub>4</sub>(<sup>153</sup>Sm, ~296 MBq) was intravenously injected into the mouse *via* tail vein, and 1 h later, the mouse was monitored by UCL, X-ray CT (Caliper), MRI (Siemens Magnetom Trio), and SPECT (Bioscan). The UCL imaging instrument was set up by our lab. The mouse was irradiated by a 980 nm laser with a power density of 50 mW/cm<sup>2</sup>. For the X-ray CT imaging using quantum FX, a scan lasted about 1 min. A modified Feldkamp algorithm, using undersampling to reduce noise, was applied to the scan data, resulting in reconstructed 3D data sets with a voxel size of 20  $\mu$ m. The MRI imaging was performed according to previous reports,<sup>55</sup> using a  $T_1$ -weighted sequence (TR = 40 ms, TE = 2.96 ms, flip angle = 60°, 256 × 256 matrix, slice thickness = 2.0 mm). SPECT images were obtained in 24 projections over 30 min using a four-head scanner with multipinhole collimators. SPECT acquisition and images were reconstructed with InVivoScope software.<sup>56</sup> The amount of the NaLuF<sub>4</sub>:Yb,Tm@NaGdF<sub>4</sub>(<sup>153</sup>Sm) in tumor was quantified using the SPECT data. All data have been processed with attenuation correction.

**Confocal Imaging of the Paraffin Section of Tumor Tissue.** The mice were sacrificed, and the tumor was excised out and fixed in paraformaldehyde, embedded in paraffin, sectioned, and stained with hematoxylin and eosin. The histological sections were observed under a confocal microscope (Olympus).

**Conflict of Interest:** The authors declare no competing financial interest.

**Acknowledgment.** This work was supported by State Key Basic Research Program of China (2012CB932403 and 2011AA03A407), National Science Foundation of China (21231004 and 21375024), Shanghai Sci. Tech. Comm. (12JC1401300 and 13NM1401101).

**Supporting Information Available:** Photo of water dispersity of 50 mg/mL in water, DLS, zeta-potential, confocal imaging of cells incubated with NaLuF<sub>4</sub>:Yb,Tm@NaGdF<sub>4</sub>(<sup>153</sup>Sm), and the tumor model. This material is available free of charge *via* the Internet at <http://pubs.acs.org>.

## REFERENCES AND NOTES

1. Louie, A. Multimodality Imaging Probes: Design and Challenges. *Chem. Rev.* **2010**, *110*, 3146–3195.
2. Lee, D. E.; Koo, H.; Sun, I. C.; Ryu, J.; Kim, K.; Kwon, I. Multifunctional Nanoparticles for Multimodal Imaging and Theragnosis. *Chem. Soc. Rev.* **2012**, *41*, 2656–2672.

3. Franc, B. L.; Acton, P. D.; Mari, C.; Hasegawa, B. H. Small-Animal SPECT and SPECT/CT: Important Tools for Preclinical Investigation. *J. Nucl. Med.* **2008**, *49*, 1651–1663.
4. Liu, Y.; Ai, K.; Lu, L. Nanoparticulate X-ray Computed Tomography Contrast Agents: From Design Validation to *In Vivo* Applications. *Acc. Chem. Res.* **2012**, *45*, 1817–1827.
5. Kim, S.; Lim, Y. T.; Soltesz, E. G.; De Grand, A. M.; Lee, J.; Nakayama, A.; Parker, J. A.; Mihaljevic, T.; Laurence, R. G.; Dor, D. M.; et al. Near-Infrared Fluorescent Type II Quantum Dots for Sentinel Lymph Node Mapping. *Nat. Biotechnol.* **2004**, *22*, 93–97.
6. Marradi, M.; Chiodo, F.; García, I.; Peñadés, S. Glyconanoparticles as Multifunctional and Multimodal Carbohydrate Systems. *Chem. Soc. Rev.* **2013**, *42*, 4728–4745.
7. Kim, J.; Piao, Y.; Hyeon, T. Multifunctional Nanostructured Materials for Multimodal Imaging, and Simultaneous Imaging and Therapy. *Chem. Soc. Rev.* **2009**, *38*, 372–390.
8. Zhou, J.; Liu, Z.; Li, F. Y. Upconversion Nanophosphors for Small-Animal Imaging. *Chem. Soc. Rev.* **2012**, *41*, 1323–1349.
9. Liu, Y.; Ai, K.; Liu, J.; Yuan, Q.; He, Y.; Lu, L. A High-Performance Ytterbium-Based Nanoparticulate Contrast Agent for *In Vivo* X-ray Computed Tomography Imaging. *Angew. Chem., Int. Ed.* **2012**, *51*, 1437–1442.
10. Xing, H. Y.; Bu, W. B.; Zhang, S. J.; Zheng, X. P.; Li, M.; Chen, F.; He, Q. J.; Zhou, L. P.; Peng, W. J.; Hua, Y. Q.; et al. Multifunctional Nanoprobes for Upconversion Fluorescence, MR and CT Trimodal Imaging. *Biomaterials* **2012**, *33*, 1079–1089.
11. Zhu, X. J.; Zhou, J.; Chen, M.; Shi, M.; Feng, W.; Li, F. Y. Core–Shell  $\text{Fe}_3\text{O}_4@\text{NaLuF}_4\text{:Yb,Er/Tm}$  Nanostructure for MRI, CT and Upconversion Luminescence Tri-modality Imaging. *Biomaterials* **2012**, *33*, 4618–4627.
12. Caravan, P.; Ellison, J. J.; McMurry, T. J.; Lauffer, R. B. Gadolinium(III) Chelates as MRI Contrast Agents: Structure, Dynamics, and Applications. *Chem. Rev.* **1999**, *99*, 2293–2352.
13. Farhanghi, M.; Holmes, R. A.; Volkert, W. A.; Logan, K. W.; Singh, A. Samarium-153-EDTMP: Pharmacokinetic, Toxicity and Pain Response Using an Escalating Dose Schedule in Treatment of Metastatic Bone Cancer. *J. Nucl. Med.* **1992**, *33*, 1451–1458.
14. Nyk, M.; Kumar, R.; Ohulchanskyy, T. Y.; Bergey, E. J.; Prasad, P. N. High Contrast *In Vitro* and *In Vivo* Photoluminescence Bioimaging Using Near Infrared to Near Infrared Upconversion in  $\text{Tm}^{3+}$  and  $\text{Yb}^{3+}$  Doped Fluoride Nanophosphors. *Nano Lett.* **2008**, *8*, 3834–3838.
15. Auzel, F. Upconversion and Anti-Stokes Processes with f and d ions in Solids. *Chem. Rev.* **2004**, *104*, 139–173.
16. Wang, G. F.; Peng, Q.; Li, Y. D. Lanthanide-Doped Nanocrystals: Synthesis, Optical–Magnetic Properties, and Applications. *Acc. Chem. Res.* **2011**, *44*, 322–332.
17. Wang, F.; Liu, X. G. Recent Advances in the Chemistry of Lanthanide-Doped Upconversion Nanocrystals. *Chem. Soc. Rev.* **2009**, *38*, 976–989.
18. Haase, M.; Schäfer, H. Upconverting Nanoparticles. *Angew. Chem., Int. Ed.* **2011**, *50*, 5808–5829.
19. Dong, H.; Sun, L. D.; Yan, C. H. Basic Understanding of the Lanthanide Related Upconversion Emissions. *Nanoscale* **2013**, *5*, 5703–5714.
20. Liu, Y.; Tu, D.; Zhu, H.; Chen, X. Lanthanide-Doped Luminescent Nanoprobes: Controlled Synthesis, Optical Spectroscopy, and Bioapplications. *Chem. Soc. Rev.* **2013**, *42*, 6924–6958.
21. Gorris, H. H.; Wolfbeis, O. S. Photon-Upconverting Nanoparticles for Optical Encoding and Multiplexing of Cells, Biomolecules, and Microspheres. *Angew. Chem., Int. Ed.* **2013**, *52*, 3584–600.
22. Xiong, L. Q.; Chen, Z. G.; Tian, Q. W.; Cao, T. Y.; Xu, C. J.; Li, F. Y. High Contrast Upconversion Luminescence Targeted Imaging *In Vivo* Using Peptide-Labeled Nanophosphors. *Anal. Chem.* **2009**, *81*, 8687–8694.
23. Liu, Q.; Feng, W.; Yang, T. S.; Yi, T.; Li, F. Y. Upconversion Luminescence Imaging of Cells and Small-Animals. *Nat. Protoc.* **2013**, *8*, 2033–2044.
24. Wang, Z. L.; Hao, J. H.; Chan, H. L. W.; Wong, W. T.; Wong, K. L. A Strategy for Simultaneously Realizing the Cubic-to-Hexagonal Phase Transition and Controlling the Small Size of  $\text{NaYF}_4\text{:Yb}^{3+},\text{Er}^{3+}$  Nanocrystals for *In Vitro* Cell Imaging. *Small* **2012**, *8*, 1863–1868.
25. Chen, G.; Shen, J.; Ohulchanskyy, T. Y.; Patel, N. J.; Kutikov, A.; Li, Z.; Song, J.; Pandey, R. K.; Ågren, H.; Prasad, P. N.; et al.  $(\alpha\text{-NaYbF}_4\text{:Tm}^{3+})/\text{CaF}_2$  Core/Shell Nanoparticles with Efficient Near-Infrared to Near-Infrared Upconversion for High-Contrast Deep Tissue Bioimaging. *ACS Nano* **2012**, *6*, 8280–8287.
26. Chatterjee, D. K.; Rufalhah, A. J.; Zhang, Y. Upconversion Fluorescence Imaging of Cells and Small Animals Using Lanthanide Doped Nanocrystals. *Biomaterials* **2008**, *29*, 937–943.
27. Park, Y. I.; Kim, J. H.; Lee, K. T.; Jeon, K. S.; Bin, H.; Yu, J. H.; Kim, H. M.; Lee, N.; Choi, S. H.; Baik, S. I.; et al. Nonblinking and Nonbleaching Upconverting Nanoparticles as an Optical Imaging Nanoprobe and  $T_1$  Magnetic Resonance Imaging Contrast Agent. *Adv. Mater.* **2009**, *21*, 4467–4471.
28. Wu, S. W.; Han, G.; Milliron, D. J.; Aloni, S.; Altoe, V.; Talapin, D. V.; Cohen, B. E.; Schuck, P. J. Non-blinking and Photo-stable Upconverted Luminescence from Single Lanthanide-Doped Nanocrystals. *Proc. Natl. Acad. Sci. U.S.A.* **2009**, *106*, 10917–10921.
29. Ostrowski, A. D.; Chan, E. M.; Gargas, D. J.; Katz, E. M.; Han, G.; Schuck, P. J.; Milliron, D. J.; Cohen, B. E. Controlled Synthesis and Single-Particle Imaging of Bright, Sub-10 nm Lanthanide-Doped Upconverting Nanocrystals. *ACS Nano* **2012**, *6*, 2686–2692.
30. Dong, C. H.; van Veggel, F. C. J. M. Cation Exchange in Lanthanide Fluoride Nanoparticles. *ACS Nano* **2009**, *3*, 123–130.
31. Liu, Y. S.; Tu, D. T.; Zhu, H. M.; Li, R. F.; Luo, W. Q.; Chen, X. Y. A Strategy To Achieve Efficient Dual-Mode Luminescence of  $\text{Eu}^{3+}$  in Lanthanides Doped Multifunctional  $\text{NaGdF}_4$  Nanocrystals. *Adv. Mater.* **2010**, *22*, 3266–3271.
32. Cheng, L.; Yang, K.; Li, Y.; Chen, J.; Wang, C.; Shao, M.; Lee, S. T.; Liu, Z. Facile Preparation of Multifunctional Upconversion Nanoprobes for Multimodal Imaging and Dual-Targeted Photothermal Therapy. *Angew. Chem., Int. Ed.* **2011**, *50*, 7385–7389.
33. Paik, T.; Gordon, T.; Prantner, A.; Yun, H.; Murray, C. Designing Tripodal and Triangular Gadolinium Oxide Nanoplates and Self-Assembled Nanofibrils as Potential Multimodal Bioimaging Probes. *ACS Nano* **2013**, *7*, 2850–2859.
34. Ren, G.; Zeng, S.; Hao, J. Tunable Multicolor Upconversion Emissions and Paramagnetic Property of Monodispersed Bifunctional Lanthanide-Doped  $\text{NaGdF}_4$  Nanorods. *J. Phys. Chem. C* **2011**, *115*, 20141–20147.
35. Hou, Y.; Qiao, R.; Fang, F.; Wang, X.; Dong, C.; Liu, K.; Liu, C.; Liu, Z.; Lei, H.; Wang, F.; et al.  $\text{NaGdF}_4$  Nanoparticle-Based Molecular Probes for Magnetic Resonance Imaging of Intrapерitoneal Tumor Xenografts *In Vivo*. *ACS Nano* **2013**, *7*, 330–338.
36. Park, Y. I.; Kim, H. M.; Kim, J. H.; Moon, K. C.; Yoo, B.; Lee, K. T.; Lee, N.; Choi, Y.; Park, W.; Ling, D.; et al. Theranostic Probe Based on Lanthanide-Doped Nanoparticles for Simultaneous *In Vivo* Dual-Modal Imaging and Photodynamic Therapy. *Adv. Mater.* **2012**, *24*, 5755–5761.
37. Kumar, R.; Nyk, M.; Ohulchanskyy, T. Y.; Flask, C. A.; Prasad, P. N. Combined Optical and MR Bioimaging Using Rare Earth Ion Doped  $\text{NaYF}_4$  Nanocrystals. *Adv. Funct. Mater.* **2009**, *19*, 853–859.
38. Chen, G.; Ohulchanskyy, T. Y.; Kumar, R.; Ågren, H.; Prasad, P. N. Ultrasmall Monodisperse  $\text{NaYF}_4\text{:Yb}^{3+},\text{Tm}^{3+}$  Nanocrystals with Enhanced Near-Infrared to Near-Infrared Upconversion Photoluminescence. *ACS Nano* **2010**, *4*, 3163–3168.
39. Ju, Q.; Tu, D.; Liu, Y.; Li, R.; Zhu, H.; Chen, J.; Chen, Z.; Huang, M.; Chen, X. Amine-Functionalized Lanthanide-Doped  $\text{KGdF}_4$  Nanocrystals as Potential Optical/Magnetic Multimodal Bioprobes. *J. Am. Chem. Soc.* **2011**, *134*, 1323–1330.

40. He, M.; Huang, P.; Zhang, C. L.; Hu, H. Y.; Bao, C. C.; Gao, G.; He, R.; Cui, D. X. Dual Phase-Controlled Synthesis of Uniform Lanthanide-Doped  $\text{NaGdF}_4$  Upconversion Nanocrystals via An OA/Ionic Liquid Two-Phase System for *In Vivo* Dual-Modality Imaging. *Adv. Funct. Mater.* **2011**, *21*, 4470–4477.

41. Lee, J.; Lee, T.; Ryu, J.; Hong, S.; Kang, M.; Im, K.; Kang, J.; Lim, S.; Park, S.; Song, R. RGD Peptide-Conjugated Multimodal  $\text{NaGdF}_4\text{:Yb}^{3+}/\text{Er}^{3+}$  Nanophosphors for Upconversion Luminescence, MR, and PET Imaging of Tumor Angiogenesis. *J. Nucl. Med.* **2013**, *54*, 96–103.

42. Ajithkumar, G.; Benjamin, Y.; Dara, E. G.; Peter, J. H.; Ai-Ling, L.; Uma, L.; Vinayak, P. D.; Dhiraj, K. S. Multimodal Bioimaging Using a Rare Earth Doped  $\text{Gd}_2\text{O}_3\text{:Yb/Er}$  Phosphor with Upconversion Luminescence and Magnetic Resonance Properties. *J. Mater. Chem.* **2013**, *1*, 1561.

43. Liu, Z.; Pu, F.; Huang, S.; Yuan, Q.; Ren, J.; Qu, X. Long-Circulating  $\text{Gd}_2\text{O}_3\text{:Yb}^{3+}, \text{Er}^{3+}$  Up-conversion Nanoprobe as High-Performance Contrast Agents for Multi-modality Imaging. *Biomaterials* **2013**, *34*, 1712–1721.

44. Chen, F.; Bu, W. B.; Zhang, S. J.; Liu, X. H.; Liu, J. N.; Xing, H. Y.; Xiao, Q. F.; Zhou, L. P.; Peng, W. J.; Wang, L. Z.; *et al.* Positive and Negative Lattice Shielding Effects Co-existing in Gd (III) Ion Doped Bifunctional Upconversion Nanoprobes. *Adv. Funct. Mater.* **2011**, *21*, 4285–4294.

45. Vetrone, F.; Naccache, R.; Mahalingam, V.; Morgan, C. G.; Capobianco, J. A. The Active-Core/Active-Shell Approach: A Strategy To Enhance the Upconversion Luminescence in Lanthanide-Doped Nanoparticles. *Adv. Funct. Mater.* **2009**, *19*, 2924–2929.

46. Wang, F.; Wang, J.; Liu, X. Direct Evidence of a Surface Quenching Effect on Size-Dependent Luminescence of Upconversion Nanoparticles. *Angew. Chem., Int. Ed.* **2010**, *49*, 7456–7460.

47. Chen, G.; Ohulchansky, T. Y.; Law, W. C.; Ågren, H.; Prasad, P. N. Monodisperse  $\text{NaYbF}_4\text{:Tm}^{3+}/\text{NaGdF}_4$  Core/Shell Nanocrystals with Near-Infrared to Near-Infrared Upconversion Photoluminescence and Magnetic Resonance Properties. *Nanoscale* **2011**, *3*, 2003–2008.

48. Liu, Q.; Sun, Y.; Yang, T. S.; Feng, W.; Li, C. G.; Li, F. Y. Sub-10 nm Hexagonal Lanthanide-Doped  $\text{NaLuF}_4$  Upconversion Nanocrystals for Sensitive Bioimaging *In Vivo*. *J. Am. Chem. Soc.* **2011**, *133*, 17122–17125.

49. Sun, Y.; Peng, J. J.; Feng, W.; Li, F. Y. Upconversion  $\text{NaLuF}_4\text{:Yb,Tm}$  Nanophosphors for Real-Time Upconversion Luminescence Imaging under Ambient Light and High-Resolution X-ray CT Imaging. *Theranostics* **2013**, *3*, 346–353.

50. Zhou, J.; Zhu, X. J.; Chen, M.; Sun, Y.; Li, F. Y. Water-Stable  $\text{NaLuF}_4$ -Based Upconversion Nanophosphors with Long-Term Validity for Multimodal Lymphatic Imaging. *Biomaterials* **2012**, *33*, 6201–6210.

51. Wang, F.; Han, Y.; Lim, C. S.; Lu, Y. H.; Wang, J.; Xu, J.; Chen, H. Y.; Zhang, C.; Hong, M. H.; Liu, X. G. Simultaneous Phase and Size Control of Upconversion Nanocrystals through Lanthanide Doping. *Nature* **2010**, *463*, 1061–1065.

52. Singh, S. K.; Kumar, K.; Rai, S. B.  $\text{Er}^{3+}/\text{Yb}^{3+}$  Codoped  $\text{Gd}_2\text{O}_3$  Nano-phosphor for Optical Thermometry. *Sens. Actuators, A* **2009**, *149*, 16–20.

53. Mai, H. X.; Zhang, Y. W.; Si, R.; Yan, Z. G.; Sun, L. D.; You, L. P.; Yan, C. H. High-Quality Sodium Rare-Earth Fluoride Nanocrystals: Controlled Synthesis and Optical Properties. *J. Am. Chem. Soc.* **2006**, *128*, 6426–6436.

54. Li, Z. Q.; Zhang, Y. An Efficient and User-Friendly Method for the Synthesis of Hexagonal-Phase  $\text{NaYF}_4\text{:Yb,Er/Tm}$  Nanocrystals with Controllable Shape and Upconversion Fluorescence. *Nanotechnology* **2008**, *19*, 345606.

55. Cao, T. Y.; Yang, T. S.; Gao, Y.; Yang, Y.; Hu, H.; Li, F. Y. Water-Soluble  $\text{NaYF}_4\text{:Yb/Er}$  Upconversion Nanophosphors: Synthesis, Characteristics and Application in Bioimaging. *Inorg. Chem. Commun.* **2010**, *13*, 392–394.

56. Zhou, J.; Sun, Y.; Du, X. X.; Xiong, L. Q.; Hu, H.; Li, F. Y. Dual-Modality *In Vivo* Imaging Using Rare-Earth Nanocrystals with Near-Infrared to Near-Infrared (NIR-to-NIR) Upconversion Luminescence and Magnetic Resonance Properties. *Biomaterials* **2010**, *31*, 3287–3295.

57. Liu, Q.; Sun, Y.; Li, C. G.; Zhou, J.; Li, C. Y.; Yang, T. S.; Zhang, X. Z.; Yi, T.; Wu, D. M.; Li, F. Y.  $^{18}\text{F}$ -Labeled Magnetic-Upconversion Nanophosphors *via* Rare-Earth Cation-Assisted Ligand Assembly. *ACS Nano* **2011**, *5*, 3146–3157.

58. Brooks, R. A.; Di Chiro, G. Principles of Computer Assisted Tomography (CAT) in Radiographic and Radioisotopic Imaging. *Phys. Med. Biol.* **1976**, *21*, 689–732.

59. Carmeliet, P. Angiogenesis in Life, Disease and Medicine. *Nature* **2005**, *438*, 932–936.

60. Jubb, A. M.; Oates, A. J.; Holden, S.; Koeppen, H. Predicting Benefit from Anti-angiogenic Agents in Malignancy. *Nat. Rev. Cancer* **2006**, *6*, 626–635.

61. Iagaru, A.; Chen, X.; Gambhir, S. Molecular Imaging Can Accelerate Anti-angiogenic Drug Development and Testing. *Nat. Clin. Pract. Oncol.* **2007**, *4*, 556–557.

62. Mulder, W.; Castermans, K.; van Beijnum, J.; Oude Egbrink, M.; Chin, P.; Fayad, Z.; Löwik, C.; Kaijzel, E.; Que, I.; Storm, G.; *et al.* Molecular Imaging of Tumor Angiogenesis Using  $\alpha\sqrt{\beta}_3$ -Integrin Targeted Multimodal Quantum Dots. *Angiogenesis* **2009**, *12*, 17–24.

63. Cai, W.; Chen, X. Multimodality Molecular Imaging of Tumor Angiogenesis. *J. Nucl. Med.* **2008**, *49*, 113S–28S.

64. Tu, D.; Liu, Y.; Zhu, H.; Chen, X. Optical/Magnetic Multimodal Bioprobes Based on Lanthanide-Doped Inorganic Nanocrystals. *Chem.—Eur. J.* **2013**, *19*, 5516–5527.

65. Liu, Y.; Tu, D.; Zhu, H.; Ma, E.; Chen, X. Lanthanide-Doped Luminescent Nano-bioprobes: From Fundamentals to Biodetection. *Nanoscale* **2013**, *5*, 1369–1384.

66. de Bazeilaire, C. M.; Duhamel, G. D.; Rofsky, N. M.; Alsop, D. C. MR Imaging Relaxation Times of Abdominal and Pelvic Tissues Measured *in Vivo* at 3.0 T: Preliminary Results. *Radiology* **2004**, *230*, 652–659.

67. Bogdan, N.; Vetrone, F.; Ozin, G. A.; Capobianco, J. A. Synthesis of Ligand-Free Colloidally Stable Water Dispersible Brightly Luminescent Lanthanide-Doped Upconverting Nanoparticles. *Nano Lett.* **2011**, *11*, 835–840.

68. Sun, Y.; Liu, Q.; Peng, J. J.; Feng, W.; Zhang, Y. J.; Yang, P. Y.; Li, F. Y. Radioisotope Post-labeling Upconversion Nanophosphors for *In Vivo* Quantitative Tracking. *Biomaterials* **2013**, *34*, 2289–2295.